Journal of Sol-Gel Science and Technology (2026) 119:26
https://doi.org/10.1007/s10971-026-07220-1

ORIGINALPAPER

Superior photocatalytic efficiency of visible-light-driven metal oxide–$BiVO_4$ heterostructure on degradation for nitroaromatic pollutants

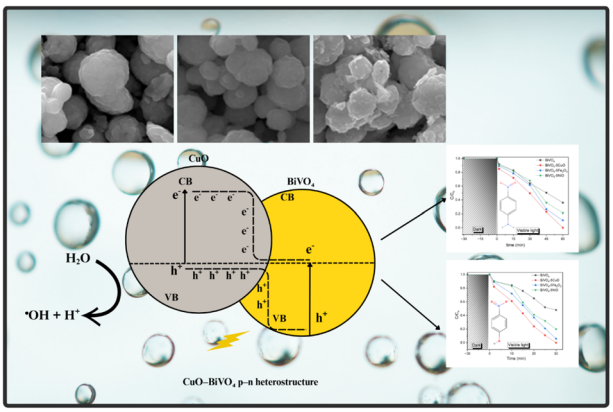
Eda Sınırtaş Ilkme[1] · Gulin Selda Pozan Soylu[1]

Received: 22 February 2026 / Accepted: 8 July 2026
© The Author(s) 2026

Abstract

$BiVO_4$ was synthesized via the hydrothermal method at different temperatures. Metal oxide (CuO, NiO, Fe_2O_3) modified $BiVO_4$ nanocomposites were prepared using the impregnation method and then X-ray diffraction (XRD), diffuse reflectance spectroscopy (DRS), Brunauer–Emmett–Teller (BET), scanning electron microscopy (SEM), photoluminescence spectroscopy (PL) and other techniques. The photocatalytic degradation mechanism for nitroaromatic pollutants was analyzed by Liquid Chromatography-Mass/Mass Spectrometry (LC-MS/MS) technique. The results show that metal oxides successfully entered the $BiVO_4$ lattice structure; the composites exhibit strong interactions, narrow band gaps, and small particle sizes, which improve visible-light absorption. Due to the synergistic effect between metal oxide and $BiVO_4$, which causes weak recombination of electron-hole pairs and high photon efficiency. The nanocomposites exhibited significantly enhanced photocatalytic properties under light irradiation. The highest degradation efficiency was obtained with the $BiVO_4$(pH 2-100 °C) at 100 °C. The addition of CuO to the $BiVO_4$ structure improved the photocatalytic degradation performance of nitroaromatic compounds. Complete degradation of 4-nitrophenol (4-NP) was achieved in 30 min, and 4-nitroaniline (4-NA) was completely degraded in 60 min with $BiVO_4$-5CuO. $BiVO_4$-5CuO nanocomposite exhibits the highest photodegradation rate for 4-NP (1.30 min^{-1}) and 4-NA (1.41 min^{-1}). This work presents the synthesis of a novel nanocomposite, which has a spherical-like morphology, that exceptionally enhances the charge-carrying ability and thereby accelerates the photocatalytic degradation of nitrophenols.

Graphical Abstract



✉ Gulin Selda Pozan Soylu
gpozan@iuc.edu.tr

[1] Department of Chemical Engineering, Faculty of Engineering, Istanbul University-Cerrahpaşa, Istanbul, Turkey

Published online: 11 August 2026

Keywords 4-Nitrophenol · 4-Nitroaniline · $BiVO_4$ · Photocatalysis · Degradation · Visible light

Highlights

- Metal oxide doping to $BiVO_4$ significantly influenced nanoparticle morphologies, optical properties and the degradation efficiency.
- $BiVO_4$-5CuO hybrid composite achieved complete 4-NP and 4-NA rapid degradation in a short time under visible light.
- Enhanced photocatalytic activity due to reduced band gap energy, increased surface area, and decreased electron-hole recombination rates.
- Metal oxide-$BiVO_4$ heterostructure holds potential for developing efficient and stable photocatalysts for environmental remediation.

1 Introduction

Efforts to treat contaminated water are increasing worldwide. Clean water is a necessary component for the survival of all life forms. Therefore, removing contaminants from wastewater is crucial for environmental protection. In this context, nitroaromatic compounds represent one of the largest and most important classes of industrial organic pollutants. These compounds are organic molecules consisting of at least one nitro functional group (-NO_2) attached to an aromatic ring, such as nitrobenzene, nitrotoluenes, nitrophenols, etc. [1].

Therefore, they are used as building block chemicals to synthesize various industrial products (e.g., dyes, cosmetics, insecticides, herbicides, fungicides, pharmaceuticals, polymers, plastics, pesticides, preservatives, antioxidants, solvents, gasoline additives, corrosion inhibitors, drugs, explosives, and others) and are synthesized in large quantities due to their high demand worldwide. According to the studies, approximately 65,000 nitroaromatic pollutants are produced as starting materials, precursors, or intermediates from different chemical industries and/or sources. The estimated annual production of nitroaromatic compounds is 108 tons [2].

Nitroaromatic compounds are a noxious waste and a persistent pollutant with chemically persistent, hazardous, and harmful effects. Due to their serious effects on human health and ecosystems, these priority pollutants that need to be reduced in the environment are listed by the US EPA. Long-term exposure to these compounds has been reported as a serious public concern for human health and food safety. These compounds, which pose a hazard to humans and other living organisms, pollute water and soil as well as air [3]. Given the importance of the potential hazards from nitroaromatic pollutants, their emissions from indoor and outdoor environments have been limited by various regulations established by primary environmental safety agencies such as the World Health Organization (WHO), the United States Environmental Protection Agency (US EPA), and the European Agency for Safety and Health at Work (EU OSHA) [4].

4-Nitrophenol (4-NP) is a common raw material used in the production of insecticides, dyes, pharmaceuticals, rubber chemicals, and fungicides. With the increase in industrial activity, organic pollutants such as 4-NP, classified as a priority pollutant, are present in large quantities in wastewater. On the other hand, 4-NP is one of the most common hazardous pollutants found in industrial, agricultural, and hospital wastewater [5].

4-nitroaniline (4-NA) is an example of a nitro compound used as a precursor for the production of a number of organic derivatives with potential applications, including corrosion inhibitors, dyes, drugs, petrochemicals, antiseptics, pesticides, plastics, pharmaceuticals, and antioxidants [6]. Due to these specialized uses, 4-NA is regularly released into water reservoirs as a major component of inadequately treated industrial wastewater. Even very low concentrations of 4-NA in water are hazardous to aquatic life and human health.

Even with traditional methods such as biological and physical treatments, more advanced technologies with lower costs and shorter time requirements are required to effectively remove contaminants [7]. Consequently, this has led to the development of efficient technologies that have replaced traditional technologies for treating industrial wastewater and contaminated clean water sources [8].

In addition to environmental pollution, another major global challenge is the energy crisis. Rising energy demand and the depletion of fossil fuel resources have driven the scientific community to explore alternative and sustainable energy sources, particularly solar and hydrogen energy. In this context, the development of novel materials, such as semiconductors capable of converting solar energy into electrical or chemical energy, has become an urgent global priority [9].

Both water pollution and energy crises are critical global issues that require sustainable technological solutions rather than solely regulatory actions. To address these problems, advanced oxidation processes (AOPs) have emerged as highly effective wastewater treatment technologies for the removal of hazardous organic compounds. [10]. AOPs

operate through the in situ generation of highly reactive hydroxyl radicals (•OH), which are primarily responsible for the oxidative degradation of organic pollutants. Owing to their strong non-selective oxidation potential, hydroxyl radicals can mineralize a wide range of organic molecules into water, carbon dioxide, and inorganic ions. The generation of hydroxyl radicals can be initiated via various pathways, including the use of strong oxidants (e.g., hydrogen peroxide and ozone), energy sources (e.g., UV light, ultrasonication, and heat), and semiconductor catalysts such as TiO_2, ZnO, and Fenton-based systems [11].

Among AOPs, photocatalysis is a promising alternative process for the degradation of emerging pollutants through oxidation under ambient temperature and pressure. Semiconductor-based photocatalysis has been widely recognized as a low-cost, sustainable, and environmentally friendly approach due to its ability to utilize solar energy [12].

Photocatalysts play an important role in water splitting for clean energy production, as well as in the degradation of organic pollutants and wastewater treatment. In particular, semiconductor photocatalytic processes have demonstrated great potential as a low-cost, environmentally friendly, and sustainable treatment technology, contributing to the development of zero-waste strategies in the drinking water and wastewater industries [13, 14].

Recent research has emphasized the critical role of catalyst structure, surface characteristics, and interfacial properties in determining catalytic activity and reaction efficiency [15–18]. In this context, rational design of catalysts through controlled surface and interface engineering has been shown to significantly enhance reaction performance by optimizing active sites and charge transfer processes. In photocatalytic systems, such structural modifications are particularly important for improving charge separation and suppressing electron–hole recombination. For instance, Liu et al. [15] reported that surface stability and adsorption energies strongly influence the formation and evolution of active surfaces, which is directly related to catalytic activity. It is well established that specific crystal facets exhibit higher reactivity, and that adsorption–desorption dynamics play a key role in determining reaction rates. Similarly, in photocatalytic processes, the formation of heterostructures has been widely recognized as an effective strategy to enhance activity. Kumar et al. [18] demonstrated that the interface between CdS and $PbWO_4$ phases effectively suppresses electron–hole recombination, leading to increased generation of reactive species.

Although numerous studies on the degradation of 4-NP and 4-NA appear in the literature, the reactions generally occur at low concentrations, radical scavengers are frequently used, and selectivity is low in terms of mineralization. Complete mineralization occurred in very few reactions. Still, there is no review reported wherein the different and most recent photocatalytic properties of $BiVO_4$ and metal oxide-doped $BiVO_4$ have been compiled and discussed extensively.

Transition metal oxides such as CuO, Fe_2O_3, and NiO have attracted significant interest in photocatalytic applications due to their favorable electronic structures, chemical stability, and cost-effectiveness. These materials contribute to enhanced photocatalytic performance, particularly by improving visible light absorption, charge carrier separation, and reactive species generation [19–22].

Synthesis conditions and the use of various additives play a crucial role in determining the photocatalytic properties and activity of $BiVO_4$-based materials. In particular, particle size, morphology, and band gap energy significantly influence visible-light-driven photocatalytic performance. Numerous studies have reported the efficient degradation of dye pollutants using metal-doped $BiVO_4$ photocatalysts [23, 24]. However, tetragonal bismuth vanadate (t-$BiVO_4$) is generally considered less active due to its relatively wide band gap, which limits its visible light response. Therefore, developing effective strategies to enhance the photoresponse and photocatalytic performance of t-$BiVO_4$ under visible light remains a critical research focus.

In this study, pure $BiVO_4$ exhibited a single monoclinic scheelite structure. To enhance its photocatalytic performance, various transition metal oxides were incorporated into the $BiVO_4$ structure for the degradation of nitroaromatic compounds. Compared to pure $BiVO_4$, the metal oxide-modified composites demonstrated reduced band gap energy, smaller crystallite size, and increased surface area, all of which contributed to improved photocatalytic activity. As a result, the photocatalytic efficiency was significantly enhanced compared to previously reported studies. Complete degradation of 4-NP was achieved within 30 min, while 4-NA was completely degraded within 60 min using the $BiVO_4$–5CuO catalyst.

Nitroaromatic compounds are generally more resistant to degradation than dye molecules due to the strong electron-withdrawing nature of the $–NO_2$ group and the high stability of the aromatic ring. Therefore, achieving complete mineralization of such compounds in photocatalytic processes remains a challenging task.

Xie et al. [25] synthesized Yb^{3+} and Tm^{3+} co-doped $BiVO_4$ by a simple hydrothermal method. This study has shown that completely degraded methylene blue in 45 min and rhodamine B solution in 90 min with the Yb-Tm/$BiVO_4$ (BVYT-3) catalyst, which has a band gap of 2.92 eV, a crystal size of 34.1 nm, and a surface area of 7.995 m^2/g.

In research, it has been reported that the photocatalytic degradation of nitroaromatic compounds (NAC) has been studied in the presence of some metal oxides and composite structures. It has been observed that these catalysts have long reaction times and low degradation efficiency in the literature. In addition, no study has been found with a semiconductor that can be effective in visible light and

Table 1 Photocatalysts used for the degradation of 4-NP and their photocatalytic activities

Catalyst	Time (min)	Degradation, %	Refs
TiO_2	120	99.9	[15]
TiO_2 (P25)	180	100	[16]
Ag/TiO_2	90	100	[17]
$BiVO_4/RGO/Ag_3PO_4$	45	82.1	[18]
Fe_3O_4-SiO_2-ZnO	180	100	[19]
$BiVO_4$	60	100	This study

Table 2 Photocatalysts used for the degradation of 4-NA and their photocatalytic activities

Catalyst	Time (min)	Degradation, %	Refs
TiO_2	180	98	[20]
TiO_2 (P25)	240	87	[21]
$Ni/ZnSn(OH)_6$	100	60	[22]
$CuO/zeolit + H_2O_2$	180	96	[23]
Au-Ag	120	100	[24]
$BiVO_4$	60	100	This study

completely degrade in a short time, such as a $BiVO_4$ photocatalyst. Some catalysts and their activities used in the photocatalytic degradation of 4-NP and 4-NA are presented in Tables 1 and 2.

This study aimed to improve environmental remediation efficiency by enhancing the photocatalytic degradation and mineralization of nitrophenols through the incorporation of various transition metal oxides into the $BiVO_4$ structure. The synthesized materials were comprehensively characterized using X-ray diffraction (XRD), Brunauer–Emmett–Teller (BET) surface area analysis, scanning electron microscopy (SEM), diffuse reflectance spectroscopy (DRS), and photoluminescence (PL) spectroscopy. Furthermore, the reaction intermediates and products were monitored by high-performance liquid chromatography (HPLC), and the resulting data were systematically analyzed to evaluate the photocatalytic performance of the prepared catalysts. The integration of $BiVO_4$ with transition metal oxides resulted in a novel composite system with significantly enhanced photocatalytic degradation performance, providing valuable insights into the development of efficient, stable, and environmentally friendly materials for pollutant removal.

2 Experimental

2.1 Materials

The precursors used in this study were commercially on hand and used without further purification treatment as follows; bismuth (III) nitrate pentahydrate (98%) and ammonium vanadate (99%) were purchased from Alfa Aesar Company, 4-nitrophenol, 4-nitroaniline and metal salts ($Cu(NO_3)_2{\cdot}3H_2O$, $Fe(NO_3)_3{\cdot}9H_2O$, $Ni(NO_3)_2{\cdot}6H_2O$) were purchased (Sigma Aldrich, 99%). The other chemicals, including nitric acid (65%), ethanol (absolute), methanol (for HPLC, ≥99%), ammonia solution (25% in water), sodium hydroxide (97%), hydroquinone, benzoquinone, and formic acid, were all purchased from Merck.

2.2 Synthesis of $BiVO_4$ photocatalyst

$BiVO_4$ structure was synthesized hydrothermally at different thermal temperatures (100, 140, and 180 °C) for 8 h in an autoclave.

0.015 mol $Bi(NO_3)_3.5H_2O$ and 0.015 mol NH_4VO_3 were dissolved in 75 mL of 2 M HNO_3 and 75 mL 6 M NaOH solutions separately, and each stirred for 0.5 h at room temperature. After that, these two mixtures were mixed together in 1:1 M ratio and stirred for about 1 h to get a stable. 65% (w/w) HNO_3 solution were then added for adjusting the pH 2 value. After the solution was placed in the autoclave. The reactions that took place during the hydrothermal synthesis are expressed by the following equations:

$$Bi(NO_3)_3 \rightarrow Bi^{3+} + 3NO_3^- \quad (1)$$

$$NH_4VO_3 \rightarrow NH_4^+ + VO_3^- \quad (2)$$

$$Bi^{3+} + VO_3^- + H_2O \rightarrow BiVO_4 + 2H^+ \quad (3)$$

After the hydrothermal treatment, the precipitates were filtered. They were then washed several times with absolute ethanol and distilled water and dried at 80 °C for 12 h. The removed moisture was calcined at 400 °C for 4 h and ground in a ball mill. This synthesized catalyst is designated as $BiVO_4$(pH 2-100 °C).

2.2.1 Synthesis of metal oxides

CuO, Fe_2O_3, and NiO structures were synthesized via the co-precipitation method. ($Cu(NO_3)_2{\cdot}3H_2O$, $Fe(NO_3)_3{\cdot}9H_2O$, $Ni(NO_3)_2{\cdot}6H_2O$) were dissolved in deionized water, and the solutions were heated to 65 °C. Then, the NH_3 solution was added dropwise to perform the precipitation. After adjusting the final pH value to 10, the solution was stirred at 65 °C for 2 h. The filtered precipitate was washed with deionized water, dried for 20 h, and calcined for 5 h.

2.3 Synthesis of metal oxide-doped $BiVO_4$ composites

Various metal oxides (CuO, Fe_2O_3, and NiO) were doped into the $BiVO_4$(pH 2-100 °C) at 1–10% by weight using the impregnation method. The powder was then dried at 110 °C for 12 h, calcined at 450 °C for 6 h, and then ground in a ball mill. This synthesized catalyst is designated as $BiVO_4$-1CuO for a 1% CuO loading, for example.

2.4 Characterization of the synthesized materials

The structures were determined using scanning electron microscopy (FE-SEM, FEI Quanta FEG-450). X-ray diffraction patterns were recorded on a Rigaku D/Max-2200 diffractometer at 40 kV with a Cu Kα radiation source ($\lambda = 1.54$ Å). The Brunauer Emmett-Teller (BET) surface area of the samples was determined using an automatic volumetric sorption analyzer (Quantachrome, Autosorb-IQ-MP). To determine band gap energy values, reflectance measurements of synthesized photocatalysts were carried out on a UV-Vis DRS (Ocean Optics, Flame Miniature Spectrometer) using a UV-Vis-NIR light source (DH-2000-BAL). During the measurements, PTFE was used as a diffuse reflectance standard. The transfer and recombination processes of photogenerated electron-holes in $BiVO_4$ samples were investigated using the photoluminescence (PL) technique. After irradiation of a photocatalyst, photons are emitted by electron-hole pair recombination, resulting in photoluminescence. PL measurement was carried out on a fluorescence spectrophotometer (Agilent Technologies-Cary Eclipse) using a Xenon lamp as the excitation source at room temperature. The sample was dispersed in ethanol using an ultrasonic bath, and the excitation wavelength used in PL measurement was 350 nm. The surface OH groups of the photocatalysts were determined by Fourier transform infrared spectroscopy. The FT-IR spectrum was recorded on a Perkin Elmer Precisely Spectrum One spectrometer at ambient conditions by using KBr as diluent. All measurements were at 4 cm^{-1} resolution and 100 scans.

2.4.1 Photocatalytic reaction methods and analytical procedure

In this study, photodegradation reactions of 4-NP and 4-NA pollutants were carried out in a 100 ml single-neck quartz reactor. Degradation reactions were carried out in a Luzchem brand reactor system under visible, UV-A, UV-B, UV-C, and halogen lamp (303-518 nm) irradiation. The light intensity of the UV lamp used for degradation experiments was recorded with the UV/Visible powermeter (SmartSensor-AR823). 50 mL of 4-NP and 4-NA solutions prepared at an initial concentration of 25 mg L^{-1} were taken, 100 mg of photocatalyst was added, and the reactions were stirred in an ultrasonic bath for 5 min. The suspension was stirred in the dark for 30 min to achieve adsorption-desorption equilibrium before illumination. After the suspension was kept under stirring and illuminated with the lamp. At certain time intervals, samples of the reaction were passed through Teflon filters (0.45 μm) to determine product distributions and were analyzed on an HPLC instrument. Acetonitrile/water (60/40) was used as the mobile phase in HPLC analysis.

The retention times of nitroaromatic compounds in the HPLC column and their possible degradation products were determined as 2.40 min for 4-NP, 2.50 min for 4-NA, 2.64 min for phenol, 1.98 min for hydroquinone, and 2.18 min for benzoquinone, respectively.

3 Results and discussion

3.1 Structural and optical analysis results of catalysts

The photocatalytic activity of the prepared catalysts was evaluated in relation to their crystallographic structure, morphology, surface characteristics, optical properties, and charge carrier dynamics, as determined by XRD, SEM, BET, DRS, PL, and FTIR analyses. Variations in crystallinity, particle size, surface area, light absorption behavior, and electron–hole recombination rates were systematically considered to explain the observed differences in photocatalytic performance.

Similar structure–activity relationships have been widely reported in the literature. Kanchana et al. [26] reported that the superior photocatalytic activity of Cu-wrapped NiO@rGO nanocomposites originated from improved surface characteristics, efficient charge separation, and enhanced interfacial interactions. Furthermore, Kistan et al. [27] showed that S-doped ZnO nanomaterials synthesized using Selenicereus undatus peel extract exhibited enhanced photocatalytic degradation of methyl orange due to structural modifications and improved optical properties that promoted the generation and utilization of photogenerated charge carriers. Consistent with these studies, the enhanced photocatalytic performance of the $BiVO_4$-based composites in the present work can be attributed to the synergistic effects of their structural and optical properties, which facilitate charge transfer, suppress electron–hole recombination, and increase the availability of active sites for photocatalytic reactions.

3.1.1 Brunauer-Emmett-Teller (BET) analysis results

Many studies have reported that the specific surface area of a photocatalyst is a key parameter influencing its

Table 3 Structural and optical properties of the photocatalysts

Catalysts	Crystallite size (nm)	Band gap (eV)	S_{BET} (m^2 g^{-1})
$BiVO_4$(pH2-100 °C)	25.1	2.57	16.25
$BiVO_4$(pH2-140 °C)	31.2	2.56	7.32
$BiVO_4$(pH2-180 °C)	35.1	2.55	5.24
$BiVO_4$–5Fe_2O_3	23.4	2.53	15.21
$BiVO_4$–5NiO	23.1	2.55	14.31
$BiVO_4$–5CuO	21.3	2.51	15.38

photocatalytic performance [28]. The BET surface area results of $BiVO_4$ samples synthesized at different temperatures are summarized in Table 3. The specific surface area of the samples decreased significantly with increasing hydrothermal synthesis temperature. Among all samples, $BiVO_4$(pH 2–100 °C) exhibited the highest surface area. This behavior can be attributed to the smaller crystal size formed under these conditions, which leads to an increased surface area. In general, higher synthesis temperatures promote sintering and the collapse of small pores, resulting in a reduction in BET surface area. The BET results are also consistent with the crystallite size trends obtained from XRD analysis.

Several studies have reported that $BiVO_4$ photocatalysts synthesized under lower pH conditions tend to exhibit higher surface areas, which in turn enhance photocatalytic degradation efficiency [29]. As shown in Table 3, the surface area of metal oxide-doped $BiVO_4$ samples is also presented. For all prepared photocatalysts, metal oxide doping did not significantly alter the specific surface area of $BiVO_4$, although a slight decreasing trend was observed.

It is generally accepted that the addition of metal species may reduce the specific surface area of catalysts. This is mainly because metal oxides can block pores and reduce their accessibility to probe molecules such as N_2, thereby affecting the measured surface area and pore volume [30].

The photocatalytic process is strongly dependent on the adsorption and desorption of reactant molecules on the catalyst surface. Although a higher surface area can provide more active sites, the number, accessibility, and distribution of these active sites are equally important for catalytic performance. Therefore, high dispersion of metal species can enhance the availability of active sites on the catalyst surface [31].

In addition to specific surface area, the behavior of photogenerated charge carriers also plays a crucial role in determining photocatalytic activity.

3.1.2 XRD analysis of nanocomposites

The crystallite sizes of the samples were calculated using the Debye–Scherrer equation ($D = K\lambda/\beta\cos\theta$). Figure 1a shows the XRD patterns of $BiVO_4$ synthesized at different temperatures under pH 2 conditions. All diffraction peaks can be indexed to the monoclinic scheelite $BiVO_4$ phase (JCPDS card no. 14-0688), confirming the formation of a single-phase structure without detectable impurities.

The strong intensity of the (121) reflection at $2\theta \approx 28.9°$ indicates high crystallinity, while peak sharpening with increasing hydrothermal temperature suggests enhanced crystal growth and increased crystallite size. This behavior is attributed to accelerated nucleation and growth kinetics at elevated temperatures, leading to particle coarsening. Accordingly, lower hydrothermal temperatures favor the formation of nanosized $BiVO_4$. Similar trends have been reported by Sun et al. [32], who observed smaller crystallites at lower synthesis temperatures under both acidic and alkaline conditions.

Figure 1b presents the XRD patterns of metal oxide-doped $BiVO_4$ samples. All samples retain the monoclinic scheelite structure, indicating that metal oxide incorporation does not alter the crystal phase. The absence of additional diffraction peaks related to CuO, NiO, or Fe_2O_3 suggests either high dispersion of dopant species or concentrations below the detection limit of XRD.

A slight shift of diffraction peaks toward lower angles is observed in doped samples, as shown in the magnified (121) reflection (Fig. 1c). This shift indicates lattice expansion induced by the incorporation of smaller metal ions (Cu^{2+}, Ni^{2+}, Fe^{3+}) compared to Bi^{3+}, suggesting successful incorporation into the $BiVO_4$ lattice, likely through interstitial incorporation.

The crystallite sizes of $BiVO_4$, $BiVO_4$–5Fe_2O_3, $BiVO_4$–5NiO and $BiVO_4$–5CuO were calculated as 25.1, 23.4, 23.1 and 21.3 nm, respectively, confirming that metal oxide incorporation suppresses grain growth and leads to smaller crystallite sizes. This behavior is consistent with peak broadening observed in XRD patterns. [33]. Reduced crystallite size and high crystallinity are known to enhance photocatalytic activity by increasing surface active sites and facilitating charge separation [34].

3.1.3 Diffuse reflectance spectroscopy (DRS) analysis results

In a semiconductor material, the band gap value indicates the energy needed to excite an electron from the valence band to the conduction band. Determining this parameter provides information on the electronic behavior of the material and its applications.

UV–Vis diffuse reflectance spectroscopy (DRS) was employed to investigate the optical properties of the synthesized semiconductor materials and to estimate their band gap energies. Reflectance measurements were performed using an Ocean Optics DH-2000-BAL light source, with a PTFE diffuse reflectance standard as reference. Figure 2a, b shows the UV-vis absorption spectra of the samples. All

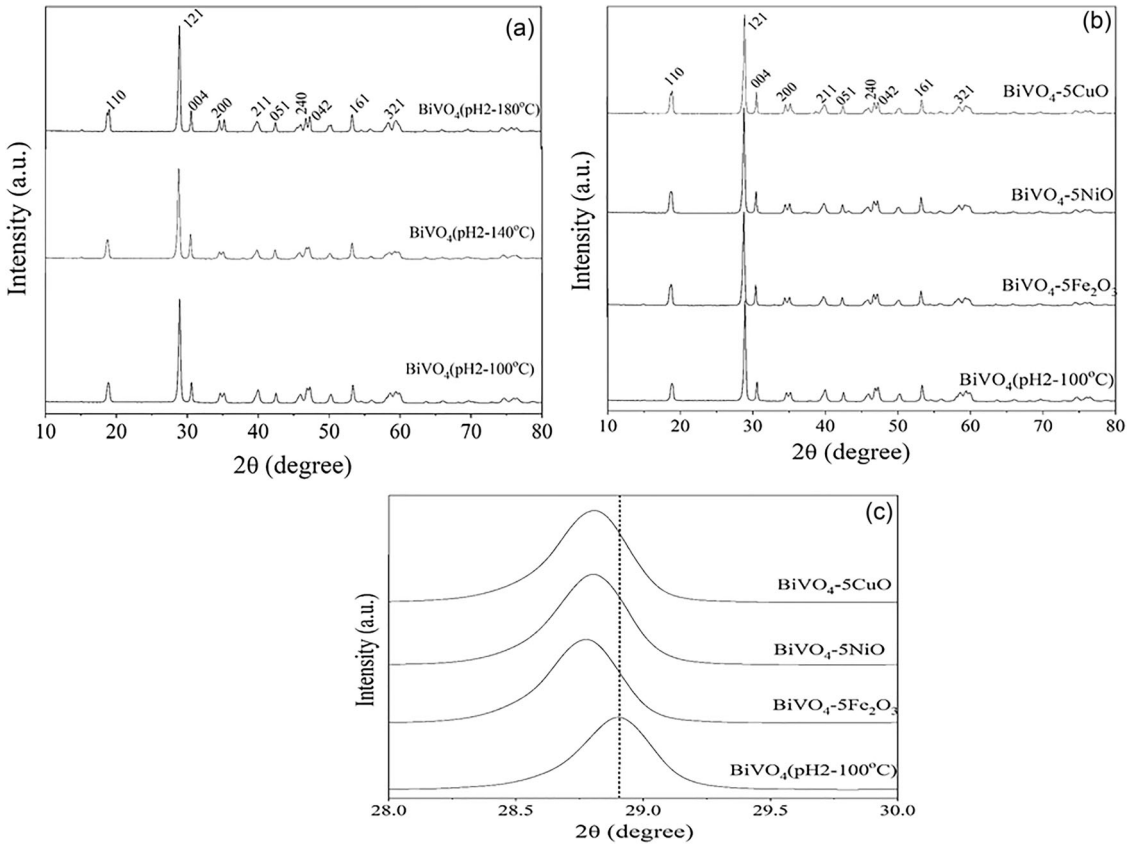


Fig. 1 XRD patterns of $BiVO_4$-based catalysts: **a** XRD patterns of $BiVO_4$ synthesized at different hydrothermal temperatures; **b** XRD patterns of pristine $BiVO_4$ and metal oxide–doped $BiVO_4$ catalysts; **c** enlarged view of the (121) diffraction peak of monoclinic $BiVO_4$

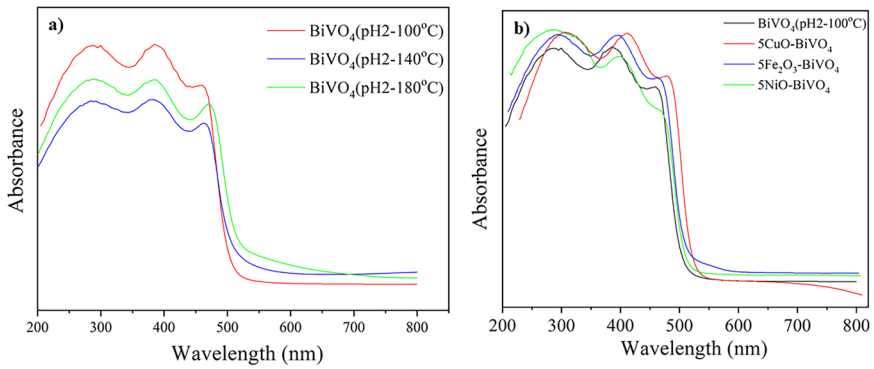


Fig. 2 UV–vis diffuse reflectance spectra of $BiVO_4$-based photocatalysts: **a** $BiVO_4$ samples synthesized at various hydrothermal temperatures; **b** $BiVO_4$ photocatalysts modified with different metal oxides

samples show excellent visible light absorption, with the CuO-doped product exhibiting the best visible light response. Results were analyzed via the Kubelka–Munk method. The band gap was then obtained through the Tauc plot. The optical band gap (E_{bg}) was calculated using the Kubelka–Munk function and the Tauc plot. [35, 36], *F(R)*, defined as:

$$F(R) = \frac{(1-R)^2}{2R} = \frac{\alpha}{s} \tag{4}$$

where R is reflectance, s is the scattering coefficient, and α is the absorption coefficient. The transformed Kubelka–Munk function, $[F(R)\cdot h\nu]1/^n$, was used to evaluate the electronic transitions, where $n = 2$ corresponds to a direct and $n = ½$ to an indirect transition. The relationship between photon energy and absorption can be expressed as:

$$(\alpha h\nu)^{1/n} = K(h\nu - Eg) \tag{5}$$

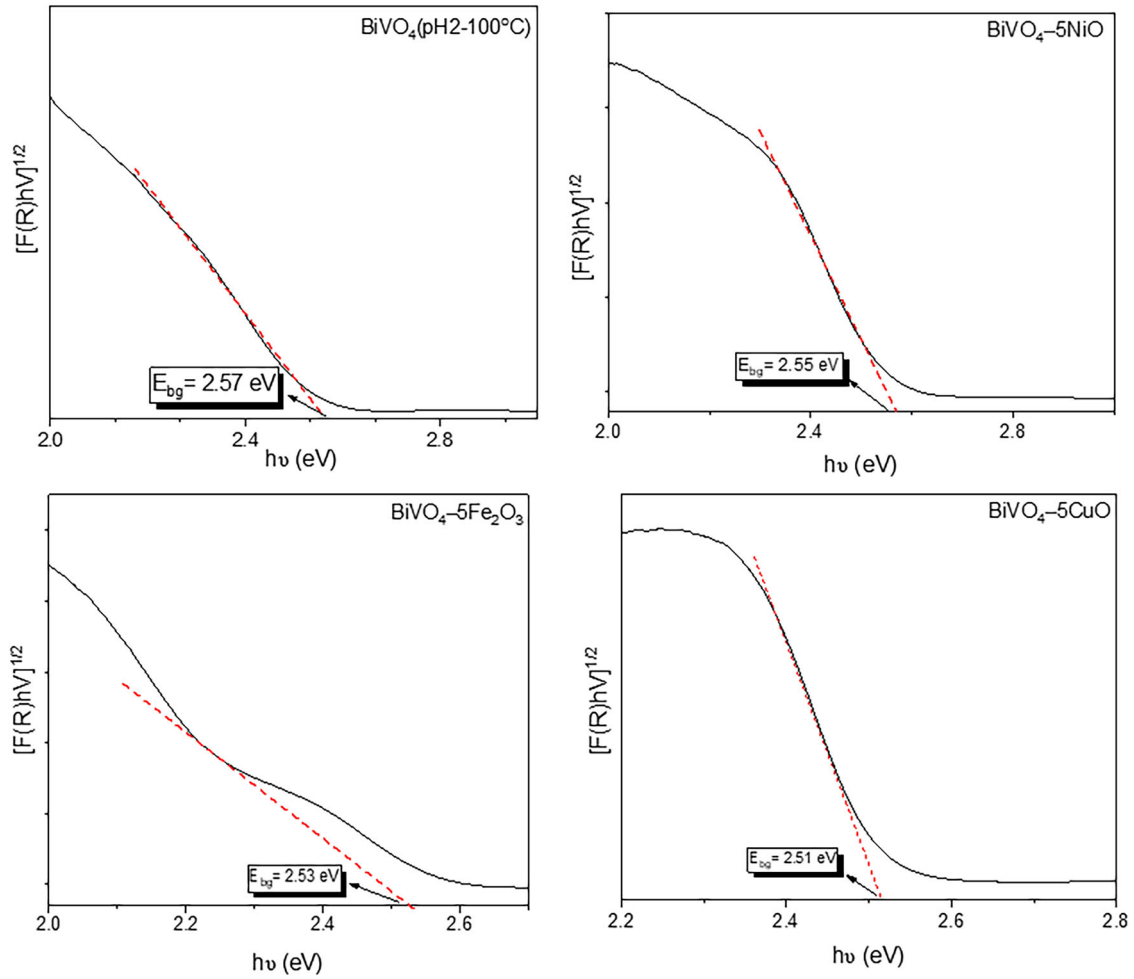


Fig. 3 Tauc's plots for the energy band gap (Eg) of the $BiVO_4$(pH2-100 °C) and metal oxide-doped $BiVO_4$ samples

where K is a material-dependent constant, h is the Planck constant (4.135×10^{-15} eV.s), and v is the Photon's frequency.

The band gap energy was determined by extrapolating the linear portion of the $[F(R)\cdot h\nu]^{1/n}$ vs. $h\nu$ plot to the x-axis, where the intercept represents E_{bg}. In this study, the constant n was taken as ½ by assuming the E_{bg} of the photocatalyst is an indirect allowed transition, and the E_{bg} values of the catalysts are shown in Fig.3.

According to the Tauc equation, the band gaps for $BiVO_4$ samples synthesized at 100 °C, 140 °C, and 180 °C were calculated as 2.57, 2.56, and 2.55 eV, respectively. Such differences in optical properties could also be due to various reasons, such as quantum confinement effects or internal lattice distortions [37]. It is thought that as the hydrothermal temperature increases, the interatomic bonds weaken and the band gap energy decreases accordingly.

In general, the electronic structure of $BiVO_4$ is proposed to consist of the valence band (VB) composed of hybridized Bi 6*s* and O 2*p* orbitals, while the conduction band (CB) consists of V 3*d* orbitals. The transition of electrons from Bi 6*s* and O 2*p* to V 3*d* corresponds to visible light, which is favorable for the photodegradation of organic pollutants under visible light irradiation. It is well known that the electronic structure of a semiconductor generally plays a very important role in its photocatalytic activity. The hybridization of Bi 6*s* and O 2*p* orbitals greatly broadens the V 6*s*, which increases the mobility of photoexcited holes and thus promotes the photocatalytic oxidation of organic pollutants [38].

In addition, the band gap energies obtained through the Tauc plot for $BiVO_4$, $BiVO_4$-5CuO, $BiVO_4$-5Fe_2O_3, and $BiVO_4$-5NiO were found to be 2.57, 2.51, 2.53, and 2.55 eV, respectively. Due to the interaction between energy levels, a shift of the absorption edges of the samples toward longer wavelengths (red shift) was observed. The decrease in the band gap indicates that the doped $BiVO_4$ samples have a larger optical absorption region than pure $BiVO_4$. The conductivity of semiconductors can be increased by doping them with an appropriate amount of

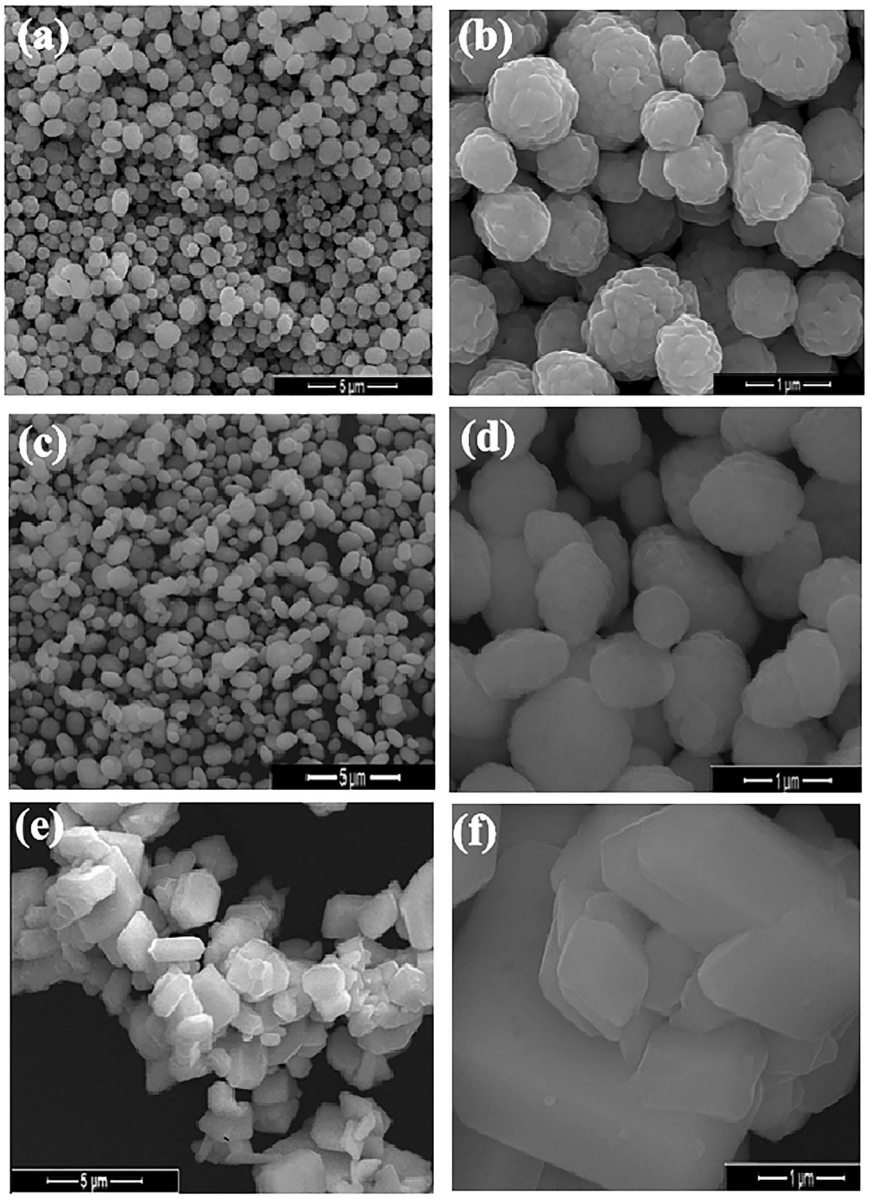


Fig. 4 SEM images of $BiVO_4$(pH 2-100 °C) (**a, b**), $BiVO_4$(pH 2-140 °C) (**c, d**), $BiVO_4$(pH 2-180 °C) (**e, f**) catalysts with 10000x (left) and 50000x (right) magnifications, respectively

metal oxide. When a semiconductor is doped, additional energy levels are generated, and the band structures may change. Therefore, the energy gap in the semiconductor decreases, and the conductivity increases further [39].

The electronic structure of semiconductors has a significant impact on their photocatalytic performance. The photodegradation performance of photocatalysts is known to be affected by the direct absorption of photon energy, allowing photoexcited electrons to migrate toward the conduction band, leaving photogenerated holes in the valence band. This separation and migration of photogenerated holes and photoexcited electrons requires the right amount of energy, or an amount greater than the band gap energy of the system, for the system to function effectively. Therefore, a visible-light-driven photocatalyst with a lower band gap energy is suitable for ensuring effective photodegradation performance.

The band gap energy for the $BiVO_4$-5CuO catalyst is lower than that of other photocatalysts, facilitating the migration of photogenerated holes and photoexcited electrons, and thus shows a better photocatalytic performance.

3.1.4 Scanning electron microscope (SEM) morphological analysis results

Figure 4 shows the SEM analysis results for $BiVO_4$. It is noticeable that the $BiVO_4$ samples synthesized at 100 and 140 °C have a spherical-like morphology, while the catalyst synthesized at 180 °C has a cuboid-like structure compared to the others. Furthermore, SEM images show that as the

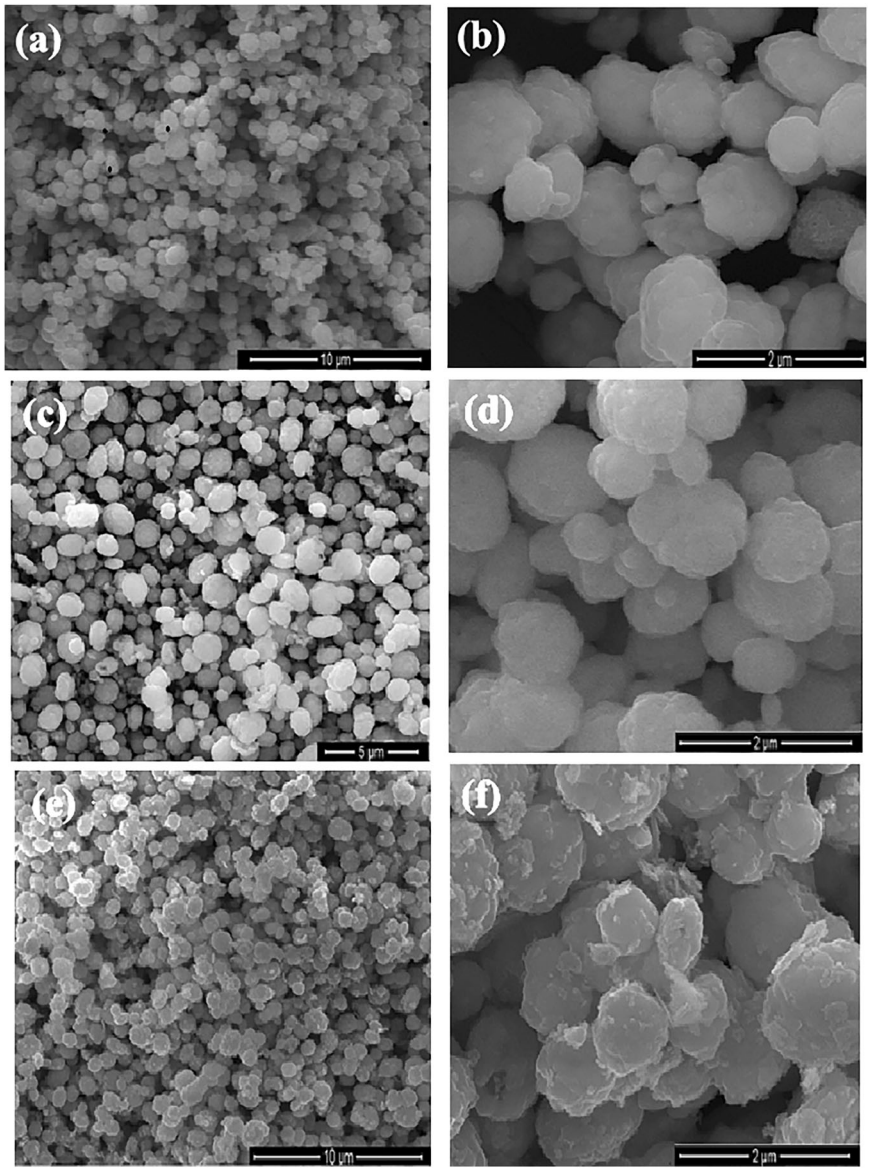


Fig. 5 SEM images of $BiVO_4$-5CuO (**a, b**), $BiVO_4$-5Fe_2O_3 (**c, d**), $BiVO_4$-5NiO (**e, f**) catalysts with 10000x (left) and 50000x (right) magnifications, respectively

hydrothermal temperature increases, the particles increase in size. This is in good agreement with XRD and surface area measurements. As is known, the reaction rate increases at higher temperatures, and crystallites grow more rapidly, resulting in larger particle sizes. Therefore, it is concluded that the hydrothermal temperature plays an important role in controlling the morphology, and that lower hydrothermal synthesis temperatures are more suitable for small-sized $BiVO_4$ catalysts.

Figure 5 shows SEM images of $BiVO_4$ photocatalysts containing various metal oxides. All metal oxide-doped $BiVO_4$ and pure $BiVO_4$ catalysts were observed to have a nearly spherical morphology. Furthermore, the particle sizes of all samples were close to each other, and a homogeneous distribution was observed on the surface. These observations support the low charge content (5%) and the small size of the metal oxide particles, their efficient distribution within the samples, and the interaction between the particles. Furthermore, the grain sizes observed in the SEM analysis were confirmed to be consistent with the results of XRD and BET analyses.

3.1.5 FT-IR analysis results

Figure 6a shows the FT-IR spectra of hydrothermally prepared $BiVO_4$ samples at various temperatures. The catalysts prepared in various variations showed characteristic vibration peaks of $BiVO_4$. All samples were characterized by a broad and strong spectrum near the 748–753 cm^{-1} range, assigned to the v3 (V-O) asymmetric stretching vibration of VO_4^{3-}, and an additional peak in the 450–500 cm^{-1} range, corresponding to v4 of VO_4^{3-}. However, shifts in these

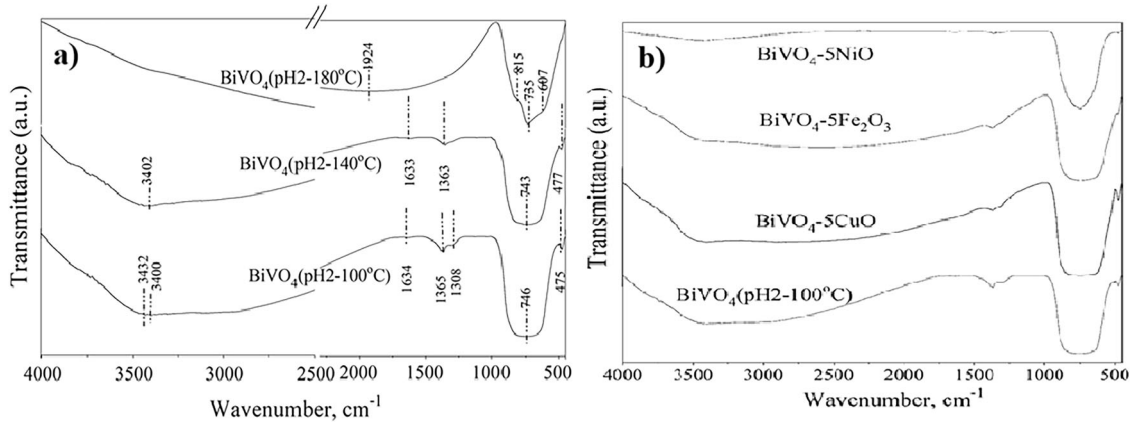


Fig. 6 FT-IR spectra of $BiVO_4$-based photocatalysts: **a** $BiVO_4$ samples synthesized at different hydrothermal temperatures; **b** metal oxide–loading $BiVO_4$ photocatalysts

bands were observed as the hydrothermal synthesis conditions varied in the samples. It is thought that the shift in the spectra of the samples may be due to the breaking of the VO_4 symmetry.

The presence of peaks around the 3400 cm^{-1} region and small band peaks in the 1000–1500 cm^{-1} range is probably due to the detection of O–H stretching and O–H bending vibrations, respectively. In other words, they represent the stretching and stretching modes of the adsorbed water molecules. The very small peaks around 1365 and 1368 cm^{-1} indicate the presence of organic impurities adsorbed on the catalyst surface. In addition, the peak around 1633–1636 cm^{-1} is attributed to the bending variation of the adsorbed water molecules [40].

The peak concentration of the OH^- group decreases with increasing temperature. Among the samples, the OH^- group concentration of $BiVO_4$(pH 2-100 °C) is higher than that of other catalysts, and this has a positive effect on the photocatalytic performance of $BiVO_4$(pH 2-100 °C) catalyst.

The three dominant peaks for $BiVO_4$(pH 2-100 °C) are stronger than those of the other synthesized catalysts, which is attributed to $BiVO_4$(pH2-100 °C) having a more active surface and OH− groups. These active site properties are crucial to highlight, as they help enhance photodegradation performance by reacting with photogenerated holes to generate more OH radicals.

Figure 6b shows the FT-IR spectra of $BiVO_4$ (pH2-100 °C) and metal oxide-doped $BiVO_4$ samples. All samples show similar spectra. The spectra of all metal oxide-doped samples are characterized by a broad and strong band assigned to the characteristic vibration peak of $BiVO_4$, around 750 (V-O). The shoulders of this band show a slight shift for the CuO, Fe_2O_3, and NiO samples. These data indicate that metal oxides are incorporated into the structure and interact with $BiVO_4$.

The presence of peaks around 3400 cm^{-1} indicates the possible presence of –OH groups. The stronger band around 3400 cm^{-1} exhibited by the CuO-supported $BiVO_4$ sample compared to the others clearly indicates the presence of more (–OH) groups. This is thought to contribute to increased photodegradation performance.

3.1.6 Photoluminescence (PL) analysis results

Figure 7a shows the PL spectra of hydrothermally prepared $BiVO_4$ samples at various temperatures around 550 nm. It is shown that the main peaks of all samples reflect at similar positions but with different intensities. Luminescence corresponds to the recombination of the hole formed in the O 2*p* band and the electron in the V 3*d* band [41].

The increase in synthesis temperature resulted in a significant enhancement in PL intensity, indicating a higher recombination rate of photogenerated electron–hole pairs. PL emission intensity is directly correlated with charge carrier recombination processes in semiconductor photocatalysts [42]. As the synthesis temperature increases, crystal growth is promoted, leading to larger crystallite sizes and a reduction in specific surface area [43]. In contrast, smaller crystallite sizes obtained at lower temperatures provide shorter migration distances and higher surface area, which favor efficient charge transfer to the surface and reduce recombination losses [44].

As a result, improved charge separation efficiency leads to enhanced photocatalytic performance. Therefore, the structural modifications in $BiVO_4$ play a crucial role in regulating charge carrier dynamics and ultimately determining its photocatalytic efficiency.

Figure 7b shows the PL spectra of metal oxide-doped $BiVO_4$ and pure $BiVO_4$ catalysts with an excitation wavelength around 550 nm. The observed trends for the PL intensities of $BiVO_4$ are $BiVO_4 > BiVO_4$-5NiO > $BiVO_4$-5Fe_2O_3 > $BiVO_4$-5CuO. PL processes are known to be affected by the dopant species and forms [45]. In this case, the transition metal oxides on the surface of the $BiVO_4$

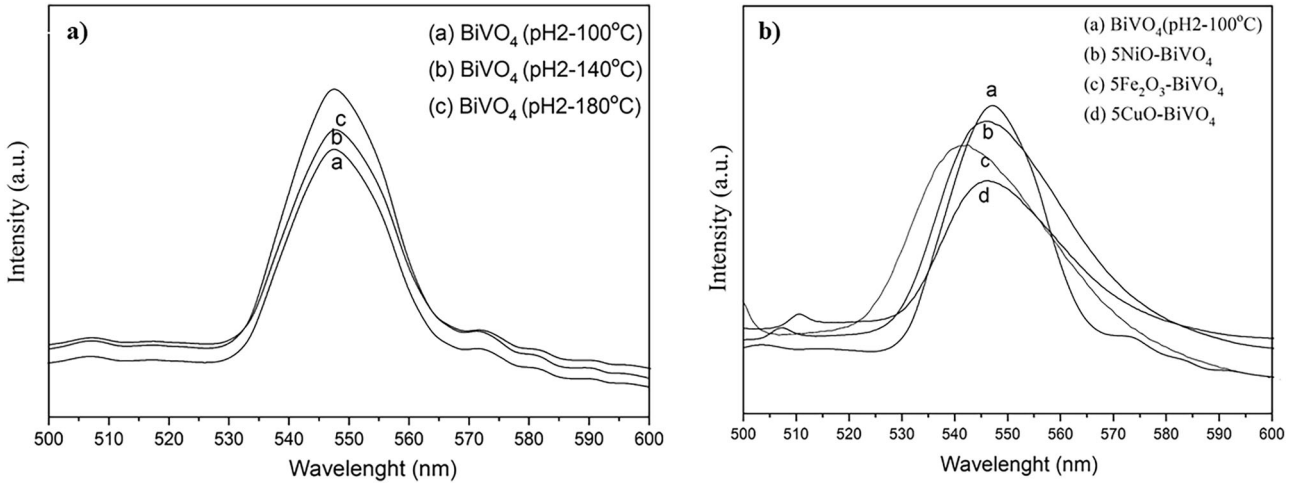


Fig. 7 PL spectra of $BiVO_4$-based photocatalysts: **a** $BiVO_4$ samples synthesized at different hydrothermal temperatures; **b** metal oxide–doped $BiVO_4$ photocatalysts

catalyst may play a role in electronic trapping in photocatalysis.

The PL spectra were quantitatively analyzed to evaluate the charge carrier recombination behavior. The maximum emission intensity of pristine $BiVO_4$ was taken as a reference ($I_0 = 1.00$), and the relative PL intensities (I/I_0) of the modified samples were estimated accordingly. The normalized intensities were determined to be approximately 0.94, 0.87, and 0.75 for $BiVO_4$–5NiO, $BiVO_4$–Fe_2O_3 and $BiVO_4$–5CuO, respectively. This corresponds to a reduction in emission intensity of about 6%, 13%, and 25%, indicating a significant suppression of electron–hole recombination upon modification. Among the samples, $BiVO_4$–5CuO exhibited the lowest PL intensity, suggesting the most efficient charge separation. This behavior can be attributed to the formation of heterojunction structures, which facilitate the modification of the samples, particularly $BiVO_4$–5CuO, which can be directly correlated with the reduced recombination rate of photogenerated charge carriers. This leads to weak recombination of electron-hole pairs and high photon efficiency. Therefore, it is expected that $BiVO_4$-5CuO can be used as a more efficient photocatalyst compared to other catalysts. The results show that the PL analysis is in good agreement with the DRS analysis data.

3.2 Photocatalytic reaction studies

The oxidation rates and efficiency of a photocatalytic system are highly dependent on a set of operational parameters that control the photodegradation of an organic molecule. Numerous studies have reported the importance of operational parameters [46].

A typical photocatalysis experiment allows the catalyst to reach an adsorption/desorption equilibrium for the substance to be degraded in the dark before starting irradiation. This simple process ensures that the photocatalyst operates at its optimum reaction rate. In the study, reactions were tested at three increasing equilibrium times (15, 30, 60) in the dark, and it was concluded that 30 min in the dark was sufficient.

Furthermore, different irradiance sources (UV-C, UV-B, UV-A, Halogen, Visible) were used for photodegradation. The presence of light within the reactor always determines the overall pollutant conversion and degradation efficiency [47]. The performances of the synthesized samples were evaluated using different light sources. UVA (8 W x 8), UVB (8 W x 8), UVC (8 W x 8), Halogen Hg Lamp (T3 120 v model, 150 W, 303-518 nm), VIS (simulated sunlight irradiation, 8 W x 8), using as the light sources without using cut-off filters. According to experimental results, it was observed that the highest photocatalytic activity for 4-NP was achieved with the $BiVO_4$(pH 2–100 °C) catalyst under visible radiation with 8 lamps, 8 mW/cm^2 radiation intensity and 64 W power density.

Oxidants such as hydrogen peroxide are important in the removal of waste pollutants for advanced oxidation processes because they are important reagents that lead to the formation of OH. These oxidants increase the number of captured electrons, which in turn generate oxidizing radicals that can inhibit recombination and thus enhance the photocatalytic degradation of the pollutant. In other words, it is widely used as an electron acceptor in photocatalytic reactions to ensure that sufficient electron collectors are available to capture the excited conduction band electron from recombination [48].

It was concluded that the oxygen in $BiVO_4$'s photodegradation performance in capturing electrons generated by light was weaker than the degradation performance in the presence of H_2O_2. The photodegradation percentage increased as the H_2O_2 amount increased from 0.10 ml to 0.15 ml. This is due to the formation of hydroxyl free radicals, which enhance photodegradation with the addition of H_2O_2. However, a slight decrease in the degradation percentage was observed when the H_2O_2 amount was increased to 0.20 ml. The use of 0.15 ml of H_2O_2 resulted in an optimum oxidant loading for the photocatalytic reaction. This is because the amount of H_2O_2 present in the reaction medium was sufficient for a given 4-nitrophenol concentration, and when used in excess, the H_2O_2 consumed was highly reactive $^{\bullet}OH$ radicals and valence band holes.

This situation is expressed by the following equations:

$$^{\bullet}OH + H_2O_2 \rightarrow HO^{\bullet}{}_2 + H_2O \quad (6)$$

$$^{\bullet}OH + HO^{\bullet}{}_2 \rightarrow O_2 + H_2O \quad (7)$$

$$\text{Catalyst}(h_{VB}{}^{+}) + H_2O_2 \rightarrow \text{Catalyst} + O_2 + 2H^{+} \quad (8)$$

$$HO^{\bullet} + HO^{\bullet} \rightarrow H_2O_2 \quad (9)$$

However, when excessive amounts of H_2O_2 are used, the oxidant can be adsorbed by the catalyst particles to modify their surfaces, thus reducing the performance of the photocatalyst [49].

These types of reactions are generally reported in the literature to conform to the pseudo-first-order kinetic model. To describe the kinetic behavior, the pseudo-first-order reaction model was considered for the reactions in the study, and the reaction rate constant (k, min^{-1}) was calculated using the formula $\ln(C_0/C_t) = kt$. Here, C_0: Initial nitroaromatic compound concentration, and C_t: Nitroaromatic compound concentration at time t.

The degradation efficiency (D%) was quantified using the equation $D\% = [(C_0 - Ct)/C_0] \times 100$, where C_0 and C_t represent initial and time-dependent absorbance, respectively.

3.2.1 Degradation of 4-NP and 4-NA

In this research, the performance of the reaction with the $BiVO_4$ catalyst under visible light was compared to that of the reactions conducted without a catalyst under visible light (photolysis) and with the catalyst alone, without any radiation source, to determine operational parameters. No significant degradation has occurred for the adsorption and photolysis processes. Among the reactions conducted under various variations, the most active activity was achieved under visible light and in the presence of the catalyst.

In literature studies, the point of zero charge (PZC) of $BiVO_4$ is around 3.5. This means that the catalyst surface is positively charged when the pH is lower than the corresponding PZC value and negatively charged when the pH is higher. The ionization state of the photocatalyst surface can be protonated and deprotonated under acidic and alkaline conditions [50]. In the current study, the pH in the reaction medium was measured as 5. In addition to the reaction pH, acidic (pH 3), neutral (pH 7), and basic (pH 9) environments were also studied. According to the data, changing the pH did not improve the degradation percentage. It was observed that the optimal result was achieved with the $BiVO_4$ catalyst at pH 5. The catalyst exhibits amphoteric character, so a positive or negative charge can develop on its surface, and therefore a pH value can influence the adsorption of pollutant molecules onto catalyst surfaces [51].

Metal oxide (CuO, NiO, Fe_2O_3) doped $BiVO_4$ catalysts were tested under visible light to improve activity in the degradation reactions of 4-NP. As shown in Fig.8, the highest degradation efficiency was observed with the CuO-doped $BiVO_4$ catalyst. This result is thought to be due to the surface and structural properties of the synthesized catalysts. The increase in charge separation efficiency increases the formation of both free hydroxyl radicals and active oxygen species [52].

This high photo-activity may be due to the abundance of hydroxyl groups present on the catalyst surface, which can prevent the electron–hole recombination by trapping the hole and generating OH radicals acting as powerful oxidants. This has been proved by the FTIR experiments.

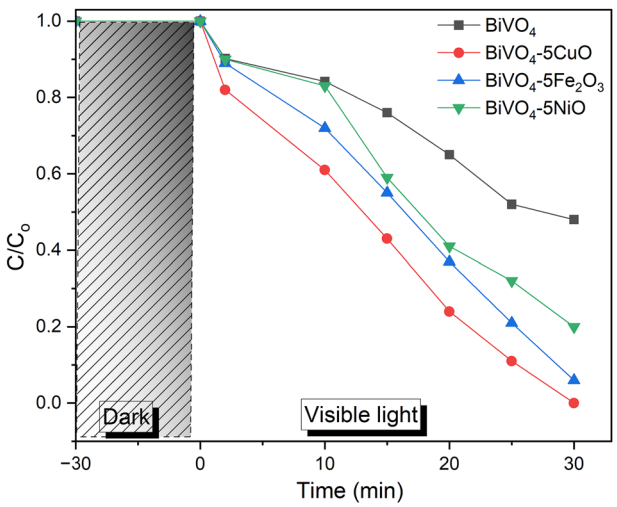


Fig. 8 . Effect of metal oxide content on the photocatalytic degradation of 4-NP over $BiVO_4$-based photocatalysts

Furthermore, the superior photocatalytic activity of the $BiVO_4$–5CuO sample compared to $BiVO_4$–5NiO and $BiVO_4$–5Fe_2O_3 can be explained based on the combined evaluation of UV–vis DRS and photoluminescence (PL) results. CuO provides relatively higher electrical conductivity and promotes faster interfacial charge transfer, further enhancing photocatalytic performance. In contrast, NiO and Fe_2O_3–modified $BiVO_4$ exhibit comparatively higher recombination rates and less effective band alignment, which limits their photocatalytic efficiency.

Therefore, the enhanced photocatalytic activity of $BiVO_4$–5CuO is attributed to its improved visible light absorption, efficient charge separation, and accelerated charge transfer properties.

The results from the photocatalytic experiments of 4-NP were fitted to the pseudo-first-order kinetic model. To compare the activities of the catalysts, photocatalytic degradation efficiencies and reaction rates were calculated, and the activity values are presented in Table 4. As shown in Table 4, the k values for in the degradation of 4-NP the $BiVO_4$(pH2-100 °C), $BiVO_4$–5NiO, $BiVO_4$–5Fe_2O_3 and $BiVO_4$-5CuO are 1.30 min^{-1}, 1.48 min^{-1}, 1.54 min^{-1}, and 1.62 min^{-1}, respectively. The results show that the degradation rate increases with the addition of 5% CuO to the $BiVO_4$ structure, and full mineralization is achieved within 30 min.

Photocatalytic reactions of the prepared doped $BiVO_4$ catalysts were also carried out to investigate the effect of various amounts of CuO doping (1, 3, 5, 7, and 10%). The degradation efficiency increases as the CuO content increases from 1% to 5%. However, a slight decrease in the degradation percentage is observed when the CuO content increases further (7% and 10%). This decrease, which occurs when a certain amount of doping is used excessively, may be due to the coating of the semiconductor surface and the closing of pores. These formations reduce the surface area available for light absorption and, consequently, the rate of photocatalytic degradation.

In addition, the reusability of the $BiVO_4$-5CuO catalyst was examined on 4-NP solution (3 trials). According to the results of the regeneration study, the catalyst was completely recovered and gave almost the same results as the fresh catalyst in the first and second regeneration steps. In the third regeneration cycle, the conversion efficiency of the catalyst decreased. After three consecutive cycles, the $BiVO_4$-5CuO catalyst achieved a degradation efficiency of 96.25% within 30 min under photocatalytic conditions. This slight decrease in the initial rate may be associated with the partial mass loss during catalyst recovery and/or the accumulation of reaction intermediates on the surface; however, achieving 100% removal again at 30 min indicates that $BiVO_4$-5CuO has good reusability. Although a slight decrease in activity was observed, the catalyst demonstrated good overall stability and reusability in photocatalytic reactions.

Additionally, the degradation reactions of 4-NA were monitored under visible light using composite structures prepared with metal oxide additives to increase activity. Figure 9 shows that complete mineralization was achieved within 60 min with the CuO-doped $BiVO_4$ catalyst. This result is thought to be due to the surface and structural properties of the synthesized catalysts.

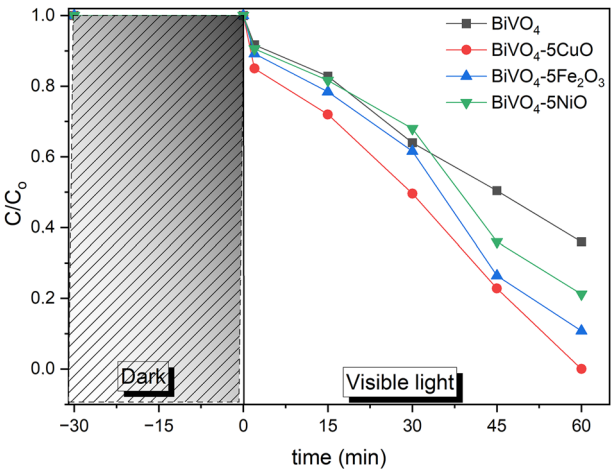


Fig. 9 Proposed pathway for photocatalytic degradation of 4-NP

Table 4 Photocatalytic efficiency and degradation kinetics of 4-NP and 4-NA over $BiVO_4$ and metal oxide-doped $BiVO_4$ catalysts under visible light irradiation

Catalyst	4-NP Degradation (%) (at 30 min)	k (min^{-1})	4-NA Degradation (%) (at 60 min)	k (min^{-1})	Regression Coefficient (R^2)
$BiVO_4$(pH2-100 °C)	52.05	1.30	64.11	1.06	0.979
$BiVO_4$(pH2-140 °C)	36.14	0.93	60.14	0.85	0.962
$BiVO_4$(pH2-180 °C)	28.47	0.87	54.22	0.81	0.978
$BiVO_4$–5NiO	80.24	1.48	79.31	1.19	0.969
$BiVO_4$–5Fe_2O_3	94.02	1.54	89.15	1.35	0.960
$BiVO_4$–5CuO	100	1.62	100	1.41	0.984

Consistent with this, Prado et al. investigated 4-nitrophenol (4-NP) degradation using a $BiVO_4$/CuO heterojunction photoelectrocatalyst and reported complete removal within 120–180 min under visible light, which was attributed to improved charge separation and reduced electron–hole recombination at the p–n heterojunction interface [53]. Similarly, Rahmati et al. studied the photodegradation of p-nitroaniline (4-NA) using a magnetic heterogeneous $AgCuFe_2O_4$@MC/AC nanophotocatalyst, and achieved 84.55% removal within 90 min under optimal conditions (pH 7, 0.04 g/L catalyst dose, 2 mg/L PS) [54].

Additionally, Karthi et al. synthesized pure $BiVO_4$ and cobalt-doped $BiVO_4$ nanocomposites and evaluated their photocatalytic performance toward the degradation of p-nitrophenol under UV irradiation. After 75 min of irradiation, the degradation efficiencies of pure $BiVO_4$ and cobalt-doped $BiVO_4$ were found to be 80% and 99.9%, respectively. The markedly higher degradation efficiency achieved by the cobalt-doped $BiVO_4$ indicates that cobalt incorporation significantly enhances the photocatalytic activity of $BiVO_4$ by promoting more effective charge separation and utilization of photogenerated charge carriers [55].

In a recent study, $BiVO_4$/PANI nanocomposites were developed for the photocatalytic degradation of p-nitrophenol under visible light irradiation. The $BiVO_4$/PANI nanocomposite exhibited superior photocatalytic performance, achieving 98.25% degradation within 240 min, whereas pristine $BiVO_4$ and PANI showed degradation efficiencies of only 53% and 49%, respectively. The enhanced activity of the nanocomposite was attributed to the synergistic interaction between $BiVO_4$ and PANI, which promoted more efficient charge separation and visible-light utilization [56].

The results from the photocatalytic experiments of 4-NA were fitted to the pseudo-first-order kinetic model. To compare the activities of the catalysts, photocatalytic degradation efficiencies and reaction rates were calculated, and the activity values are presented in Table 4. As shown in Table 4, the k values for in the degradation of 4-NA are as follows: $BiVO_4$(pH2-100 ℃), $BiVO_4$–5NiO, $BiVO_4$–$5Fe_2O_3$ and $BiVO_4$-5CuO are 1.06 min^{-1}, 1.19 min^{-1}, 1.35 min^{-1}, and 1.41 min^{-1}, respectively. According to the results, the degradation rate increased compared to the bare $BiVO_4$ structure. The addition of 5% CuO to the $BiVO_4$ structure incorporation leads to a higher degradation rate compared to other metal oxide modifications, which can be attributed to its efficient charge separation capability and enhanced generation of reactive species.

3.2.2 Degradation mechanism and pathway

The photocatalytic degradation of 4-NP and 4-NA involves light absorption by the catalyst, followed by the generation of electron–hole pairs (e^-/h^+). These charge carriers lead to the formation of reactive species such as •OH and $•O_2^-$, which attack the pollutant and convert it into intermediate products. These intermediates are further oxidized and ultimately mineralized into CO_2, H_2O, and inorganic ions.

In the case of 4-NP and 4-NA, the nitro group can be effectively removed via electrophilic attack by •OH radicals. The proposed photocatalytic degradation pathway of 4-NP and 4-NA is illustrated in Figs. 10 and 11 and is supported by intermediates identified in periodically collected samples analyzed using HPLC and LC–MS/MS. These intermediates are consistent with those reported in the literature as oxidation products of 4-NP [57].

During the photocatalytic process, phenol, hydroquinone, and benzoquinone were detected as intermediate species; however, their concentrations remained relatively low. Following their formation, the degradation proceeded through successive oxidation steps, ultimately leading to complete mineralization into CO_2, H_2O, and inorganic ions in the presence of efficient catalysts. The product distribution profiles for the degradation of 4-NP obtained with the most active catalysts are presented in Fig. 12.

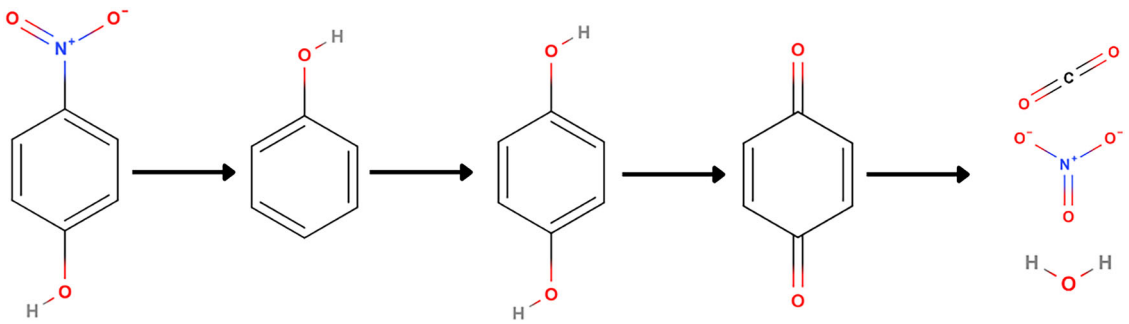


Fig. 10 Identified intermediates formed during the photocatalytic degradation of 4-NP using H_2O_2 and the 5CuO–$BiVO_4$ catalyst. The inset shows the photodegradation performance of $BiVO_4$ powders synthesized at pH 2 and 100 °C

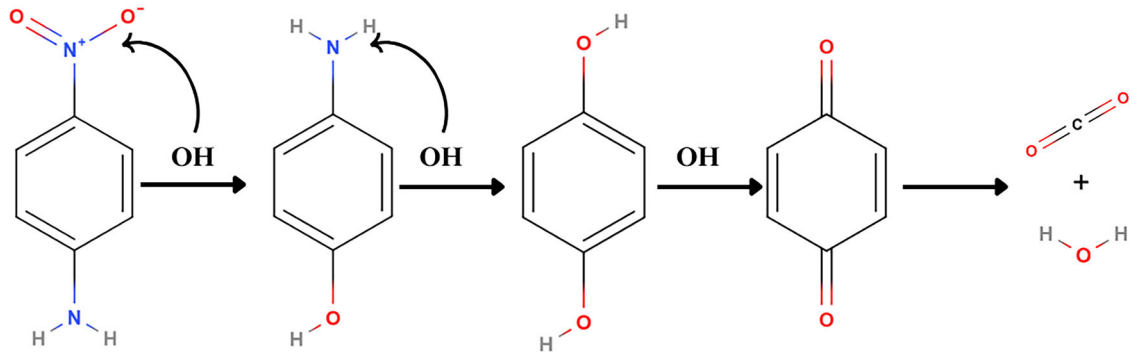


Fig. 11 Effect of metal oxide loading on the photocatalytic degradation of 4-NA over $BiVO_4$-based photocatalysts

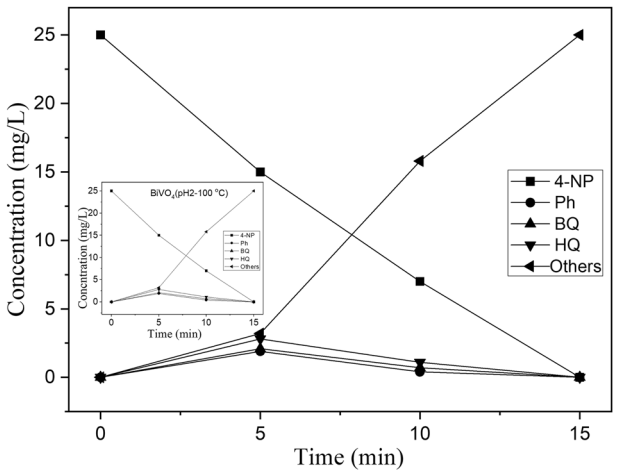


Fig. 12 Proposed pathway for photocatalytic degradation of 4-NA

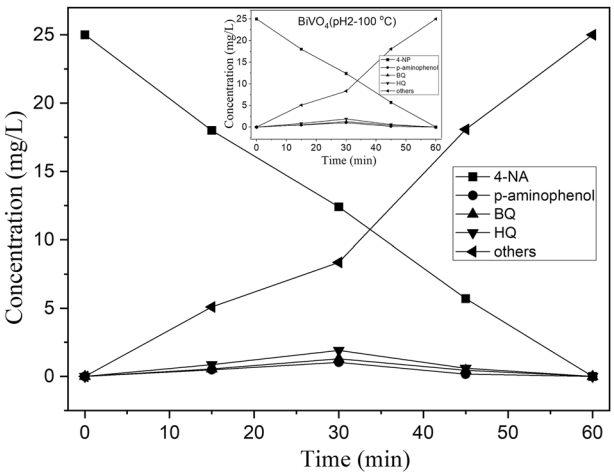


Fig. 13 Identified intermediates formed during the photocatalytic degradation of 4-NA using H_2O_2 and a 5CuO–$BiVO_4$ catalyst. The inset shows the photodegradation performance of $BiVO_4$ powders synthesized at pH 2 and 100 °C

Additionally, the photocatalytic degradation of 4-NA, p-aminophenol, hydroquinone, and p-benzoquinone was observed as intermediates, although the concentrations of these intermediates were very low. After their formation, the degradation reaction progressed, and complete mineralization was achieved with effective catalysts. It was noted that all intermediates identified in the process were hydroxylated compounds. This finding clearly demonstrates that the hydroxyl radical plays a crucial role in the degradation of 4-NA and its intermediates. The product distribution profiles of the reactions carried out with effective catalysts are shown in Fig.13.

4 Conclusion

In this study, $BiVO_4$ nanocomposite was successfully synthesized via the hydrothermal method. Metal oxide (CuO, NiO, Fe_2O_3) loaded on $BiVO_4$ was prepared using the impregnation method and employed to degrade 4-NP and 4-NA under visible light irradiation.

Metal doping into $BiVO_4$ caused a decrease in grain size, band energy, and PI density while increasing the photocatalytic activity. According to SEM and XRD analysis, it was understood that metal oxides have a strong and effective interaction with the $BiVO_4$ nanostructure. Metal oxide-doped hybrid materials, particularly the 5CuO-$BiVO_4$, demonstrated higher photocatalytic degradation of 4-NP and 4-NA pollutants than the pure $BiVO_4$. It was concluded that electron transfer from CuO to $BiVO_4$ occurred, resulting in a strong Cu-Bi-V-O bond between CuO and $BiVO_4$ through chemical interactions.

Additionally, 4-NP was completely degraded in 30 min, and 4-NA in 60 min under visible light using 5CuO-$BiVO_4$. The kinetic rate constant for 4-NP and 4-NA degradation with $BiVO_4$-5CuO was obtained as 1.62 min^{-1} and 1.41 min^{-1}, respectively, and was found to be higher than that of the $BiVO_4$.

The increased activity of the $BiVO_4$ nanostructure in the degradation reactions indicates that the CuO-doped $BiVO_4$

hybrid composite is a promising material suitable for 4-NP and 4-NA pollutants as a photocatalyst in water treatment systems.

The findings of this study demonstrate the potential of the CuO-doped $BiVO_4$ photocatalysts for the efficient degradation of nitroaromatic pollutants under visible-light irradiation. Future research should focus on improving catalyst stability and reusability, optimization studies and evaluation under real wastewater conditions would provide valuable insights into their practical feasibility. The development of cost-effective, stable, and highly active photocatalysts could contribute significantly to sustainable environmental remediation and wastewater treatment technologies.

5 Materials and methods

5.1 Ethics approval and consent to participate

This article does not contain any studies with human participants or animals performed by any of the authors.

Data availability

No datasets were generated or analysed during the current study.

Acknowledgements The authors would like to sincerely express their thanks to the Scientific Research Projects (BAP) Coordination Unit of Istanbul University-Cerrahpaşa for supporting the project under project no.: 34169.

Author contributions Gulin Selda Pozan Soylu conceived the idea, designed the experiments, edited drafted the manuscript and revised. Eda Sınırtas Ilkme conducted material synthesis, characterization experiments and carried out the major catalytic performance test. Conceptualization: Gulin Selda Pozan Soylu; Methodology: Gulin Selda Pozan Soylu; Formal analysis and investigation: Eda Sınırtas Ilkme; Writing—original draft preparation: Gulin Selda Pozan Soylu; Writing—review and editing: Gulin Selda Pozan Soylu; Resources: Gulin Selda Pozan Soylu, Eda Sınırtas Ilkme; Supervision: Gulin Selda Pozan Soylu.

Funding This study was supported by the research project number FDK-2020-34169 of the Scientific Research Projects Coordination Unit of İstanbul University-Cerrahpaşa.

Compliance with ethical standards

Conflict of interest The authors declare no competing interests.

Publisher's note Springer Nature remains neutral with regard to jurisdictional claims in published maps and institutional affiliations.

Open Access This article is licensed under a Creative Commons Attribution-NonCommercial-NoDerivatives 4.0 International License, which permits any non-commercial use, sharing, distribution and reproduction in any medium or format, as long as you give appropriate credit to the original author(s) and the source, provide a link to the Creative Commons licence, and indicate if you modified the licensed material. You do not have permission under this licence to share adapted material derived from this article or parts of it. The images or other third party material in this article are included in the article's Creative Commons licence, unless indicated otherwise in a credit line to the material. If material is not included in the article's Creative Commons licence and your intended use is not permitted by statutory regulation or exceeds the permitted use, you will need to obtain permission directly from the copyright holder. To view a copy of this licence, visit http://creativecommons.org/licenses/by-nc-nd/4.0/.

References

1. Bilal M, Bagheri AR, Bhatt P, Chen S (2021) Environmental occurrence, toxicity concerns, and remediation of recalcitrant nitroaromatic compounds. J Environ Manage 291: 112685
2. Kumar P, Kim KH, Lee J, Shang J, Khazi MI, Kumar N et al. (2019) Metal–organic framework for sorptive/catalytic removal and sensing applications against nitroaromatic compounds. J Ind Eng Chem 84:87–95
3. Gogoi D, Karmur RS, Das MR, Ghosh NN (2022) Cu and $CoFe_2O_4$ nanoparticles decorated hierarchical porous carbon: an excellent catalyst for reduction of nitroaromatics and microwave-assisted antibiotic degradation. Appl Catal B Environ 312: 121407
4. Ju KS, Parales RE (2010) Nitroaromatic compounds, from synthesis to biodegradation. Microbiol Mol Biol Rev 74(2):250–272
5. Zhang W, Tan F, Wang W, Qiu X, Qiao X, Chen J (2012) Facile, template-free synthesis of silver nanodendrites with high catalytic activity for the reduction of *p*-nitrophenol. J Hazard Mater 217–218:36–42
6. Liu YJ, Zhao ZX, Hu ZL, Liu QX (2022) A new chemodosimeter for *p*-nitroaniline based on bis-benzimidazolium salt. Tetrahedron 111: 132719
7. Saleh TA (2015) Mercury sorption by silica/carbon nanotubes and silica/activated carbon: a comparison study. J Water Supply Res Technol AQUA 64(8):892–903
8. Yahya N, Aziz F, Jamaludin NA, Mutalib MA, Ismail AF, Salleh WNW et al. (2018) A review of integrated photocatalyst adsorbents for wastewater treatment. J Environ Chem Eng 6(6):7411–7412
9. Mao M, Chen F, Zheng C, Ning J, Zhong Y, Hu Y (2016) Facile synthesis of porous Bi_2O_3–$BiVO_4$ p–n heterojunction composite microrods with highly efficient photocatalytic degradation of phenol. J Alloys Compd 688:1080–1087
10. Zheng T-H, Zhang Z-Z, Liu Y, Zou L-H (2025) Recent progress in catalytically driven advanced oxidation processes for wastewater treatment. Catalysts 15(8):761
11. Khader EH, Muslim SA, Saady NMC, Ali NS, Salih IK, Mohammed TJ, Albayati TM, Zendehboudi S (2024) Recent advances in photocatalytic advanced oxidation processes for organic compound degradation: a review. Desalination Water Treat 318: 100384
12. Wu H, Li L, Wang S, Zhu N, Li Z, Zhao L, Wang Y (2023) Recent advances of semiconductor photocatalysis for water pollutant treatment: mechanisms, materials and applications. Phys Chem Chem Phys 25:25899–25924
13. Zhang L, Wang H, Chen Z, Wong PK, Liu J (2011) Bi_2WO_6 micro/nano-structures: synthesis, modifications and visible-light-driven photocatalytic applications. Appl Catal B Environ 106(1–2):1–13

14. Oller I, Malato S, Sánchez-Pérez JA (2010) Combination of advanced oxidation processes and biological treatments for wastewater decontamination—a review. Sci Total Environ 409(20):4141–4166
15. Liu Y, Zhang Z, Han C, Ou L, Wang J, Liu C (2025) Unveiling the growth mechanism of Fe-containing intermetallics in Al–Si alloy from the perspective of surface stability and atom adsorption. J Mater Res Technol 34:123–135
16. Wang X, Li Y, Zhang Z, Chen J, Liu H, Wang Y (2024) Upgrading CO_2 to sustainable aromatics via perovskite-mediated tandem catalysis. Nat Commun 15: 1234
17. Wei J, Ge Q, Yao R, Wen Z, Fang C, Guo L, Xu H, Sun Y (2017) Nano bifunctional catalysts as miniaturized chemical processes for COx-to-aromatics conversion. Nat Commun 8: 15174
18. Kumar S, Kumar A, Bahuguna A, Sharma V, Krishnan V (2017) Fabrication of CdS–$PbWO_4$ nanocomposite to improve the photocatalytic degradation efficiency of methylene blue under visible light irradiation. J Alloys Compd 692:936–945
19. Chitra M, Kistan A, Kanchana V, Jayanthi A (2024) Sol–gel synthesis, characterization and photocatalytic activity of Cobalt-doped ZnO nanoparticles. Res J Chem Environ 28(3):48–55
20. Anbarasan V, Arivalagan K, Kalicharan AA, Kistan A (2025) Synthesis of CuO nanoparticles using *Amorphophallus paeoniifolius* tuber extract and its photocatalytic activity on malachite green dye. Res J Chem Environ 29(3):3
21. Kistan A, Priya G, Jagan Raj S, Mayavan L (2024) Improved photocatalytic activity of Ce-doped NiO nanoparticles against methylene blue and rhodamine B dyes. Ionics 31:1–14
22. Balarabe BY, Oumarou MNI, Koroney AS, Adjama I, Baraze AIR (2023) Photo-oxidation of organic dye by Fe_2O_3 nanoparticles: catalyst, electron acceptor, and polyurethane membrane (PU-Fe_2O_3) effects. J Nanotechnol 2023:12
23. Hemmatpour P, Nezamzadeh-Ejhieh A, Ershadi A (2025) A photodegradation study of the deposition fabricated CdS–$BiVO_4$ binary catalyst: a brief comparison with other fabrication procedures. Mater Adv 6:3969–3984
24. Liu F, Zhang S, Xu D, Sun F, Wang W, Li X, Yu W, Dong X, Liu G, Yu H (2022) Columnar cactus-like 2D/1D BiOBr/$BiVO_4$:Yb^{3+}, Er^{3+} heterostructure photocatalyst with ultraviolet–visible–near infrared response for photocatalytic degrading dyes, endocrine disruptors and antibiotics. J Alloys Compd 929: 167330
25. Xie H, Wang M, Sun Z, Lu X, Zhang D, Jin S, Chen S (2024) Efficient visible light photodegradation of $BiVO_4$: Yb^{3+}/Tm^{3+} with high content of tetragonal phase. Front Chem Sci Eng 18(11):122
26. Kanchana V, Kistan A, Ramesh S, Balaramesh P (2026) Green synthesis of Cu wrapped NiO@rGO nanocomposite using Acacia nilotica plant extract: a sustainable solution for photocatalytic and antioxidant activities. Waste Biomass Valor 17(4):2247–2260
27. Kistan A, Mahimairaj P, Mohan S, Jeevalatha R (2026) Novel synthesis of S-doped ZnO nanomaterials using Selenicereus undatus peel extract for enhanced UV photocatalytic degradation of methyl orange. Rasayan J Chem 9(1):575–582
28. Nainani R, Thakur P, Chaskar M (2012) Synthesis of silver-doped TiO_2 nanoparticles for the improved photocatalytic degradation of methyl orange. J Mater Sci Eng B 2(1):52–58
29. Phiankoh S, Munprom R (2018) Effect of pH on crystal structure and morphology of hydrothermally synthesized $BiVO_4$. Mater Today Proc 5(3):9447–9452
30. Pang YL, Abdullah AZ (2012) Effect of low Fe^{3+} doping on characteristics, sonocatalytic activity and reusability of TiO_2 nanotube catalysts for removal of Rhodamine B from water. J Hazard Mater 235–236:326–335
31. Li JQ, Guo ZY, Wang DF, Lui H, Du J, Zhu ZF (2012) Effects of pH value on the surface morphology of $BiVO_4$ microspheres and removal of methylene blue under visible light. J Exp Nanosci 9(6):616–624
32. Sun W, Xie M, Jing L, Luan Y, Fu H (2011) Synthesis of large surface area nano-sized $BiVO_4$ by an EDTA-modified hydrothermal process and its enhanced visible photocatalytic activity. J Solid State Chem 184(11):3050–3054
33. Walid A, Soeparman S, Wahyudi S, Sasongko MN (2021) The effect of nickel-doped bismuth vanadium oxide on microstructures and electric properties towards $BiVO_4$–NiO composite. Mater Chem Phys 265: 124452
34. Zhao W, Wang Y, Yang Y, Tang J, Yang Y (2011) Carbon spheres supported visible-light-driven CuO–$BiVO_4$ heterojunction: preparation, characterization, and photocatalytic properties. Appl Catal B Environ 115–116:90–99
35. Iyyapushpam S, Nishanthi ST, Pathinettam Padiyan D (2014) Enhanced photocatalytic degradation of methyl orange by gamma Bi_2O_3 and its kinetics. J Alloys Comp 601:85–87
36. Makuła P, Pacia M, Macyk W (2018) How to correctly determine the band gap energy of modified semiconductor photocatalysts based on UV–Vis spectra. J Phys Chem. Lett 9(23):6814–6817
37. Al-Jawad SMH, Ismail MM, Emad S (2016) Effect of hydrothermal reaction temperatures on structural and optical properties of ZnS nanoparticles. Eng Technol J 34(6B):808–819
38. Tang J, Zou Z, Ye J (2004) Efficient photocatalytic decomposition of organic contaminants over $CaBi_2O_4$ under visible-light irradiation. Angew Chem Int Ed 43(34):4463–4466
39. Trinh DTT, Khanitchaidecha W, Channei D, Nakaruk A (2019) Synthesis, characterization and environmental applications of bismuth vanadate. Res Chem Intermed 45(10):5217–5259
40. Cichosz S, Masek A (2019) Cellulose fibers hydrophobization via a hybrid chemical modification. Polymers 11(7):1174
41. Deng Y, Tang L, Zeng G, Feng C, Dong H, Wang J et al. (2017) Plasmonic resonance excited dual Z-scheme $BiVO_4$/Ag/Cu_2O nanocomposite: Synthesis and mechanism for enhanced photocatalytic performance in recalcitrant antibiotic degradation. Environ Sci Nano 4(7):1494–1511
42. Leong S, Razmjou A, Wang K, Hapgood K, Zhang X, Wang H (2014) TiO_2-based photocatalytic membranes: a review. J Membr Sci 472:167–184
43. Zhang L, Wong KH, Chen Z, Yu JC et al. (2010) AgBr–Ag–Bi_2WO_6 nanojunction system with enhanced visible-light photocatalytic activity. Appl Catal B Environ 95:93–99
44. Dong S, Feng J, Fan M, Pi Y et al. (2015) Recent developments in heterogeneous photocatalytic water treatment using visible light-responsive photocatalysts: a review. RSC Adv 5:14610–14630
45. Liqiang J, Yichun Q, Baiqi W, Shudan L, Baojiang J, Libin Y et al. (2006) Review of photoluminescence performance of nano-sized semiconductor materials and its relationships with photocatalytic activity. Sol Energy Mater Sol Cells 90(12):1773–1787
46. Kumar A, Pandey G (2017) A Review on the factors affecting the photocatalytic degradation of hazardous materials Mater Sci Eng Int J 1:106–114
47. Garcia-Segura S, Brillas E (2017) Applied photoelectrocatalysis on the degradation of organic pollutants in wastewaters. J Photochem Photobiol C Photochem Rev 31:1–35
48. Saggioro EM, Oliveira AS, Pavesi T, Maia CG, Ferreira LFV, Moreira JC (2011) Use of titanium dioxide photocatalysis on the remediation of model textile wastewaters containing azo dyes. Molecules 16(12):10370–10386
49. Sahel K, Elsellami L, Mirali I, Dappozze F, Bouhent M, Guillard C (2016) Hydrogen peroxide and photocatalysis. Appl Catal B Environ 188:106–112
50. Ambrosio F, Wiktor J, Pasquarello A (2018) pH-dependent surface chemistry from first principles: application to the $BiVO_4$(010)–water interface. ACS Appl Mater Interfaces 10(12):10011–10021

51. Akpan UG, Hameed BH (2009) Parameters affecting the photocatalytic degradation of dyes using TiO_2-based photocatalysts: a review. J Hazard Mater 170(2–3):520–529
52. Tijani JO, Fatoba OO, Madzivire G, Petrik L.F (2014) A review of combined advanced oxidation technologies for the removal of organic pollutants from water. Water, Air, and Soil Pollut 225, 2102.
53. Prado TM, Silva FL, Grosseli G, Fadini PS et al. (2020) Using $BiVO_4$/CuO-based photoelectrocatalyzer for 4-nitrophenol degradation. Materials 13(6):1322
54. Rahmati N, Hashemi M, Nasiri A (2025) Persulfate-enhanced photodegradation of para-nitroaniline in wastewater using $AgCuFe_2O_4$@MC/AC as a newly synthesized heterogeneous magnetic nanophotocatalyst: mechanism study and bioassay of effluent. Environ Technol Innov 38: 104181
55. Karthi N, Rameshkumar KA, Maadeswaran P (2024) Photocatalytic performance of pristine and cobalt-loaded $BiVO_4$ nanocomposites for effective degradation of p-nitrophenol organic pollutants. Nanotechnol Environ Eng 9:17–28
56. Jiteshwaran T, Janani B, Syed A et al. (2024) Interfacial engineering of $BiVO_4$/PANI p–n heterojunction for enhanced photocatalytic degradation of p-nitrophenol: Pathway, toxicity evaluation and mechanistic insights. Surf Interfaces 49: 104361
57. Ahn WY, Sheeley SA, Rajh T, Cropek DM (2007) Photocatalytic reduction of 4-nitrophenol with arginine-modified titanium dioxide nanoparticles. Appl Catal B Environ 74(1–2):103–110